ChemPhysChem

Research Article
doi.org/10.1002/cphc.202400140

Chemistry Europe
European Chemical Societies Publishing

www.chemphyschem.org

Density Functional Theory Calculations on Fluorescence-Enhanced Mechanisms of the Optical Sensor for Zinc Ions, ADPA

Quyan Su,[a] Yuanming Li,[a] Jia Han,[b] Xiaoguo Zhou,*[a, b] and Shilin Liu*[a, b]

N-(9-anthracenylmethyl)-N-(2-pyridinylmethyl)-2-pyridinemethanamine (ADPA) as a specific ion sensor for Zn^{2+} has been widely applied. Although the photo-induced electron transfer (PET) mechanism was proposed previously, its fluorescence-enhanced effect still remains somewhat ambiguous, according to unknown influences of non-radiative energy decay pathways, such as intersystem crossing and internal conversion. Herein, a thorough study using density functional theory has been performed for low-lying electronic states of the ADPA monomer and hydrated ADPA-Zn^{2+} complex. Based on interfragment charge transfer analyses, we quantitatively calculated the amount of transferred electrons in the monomer and complex, providing solid evidences for the PET mechanism and in line with the conclusion of frontier molecular orbital analyses. Moreover, the ISC process of $S_1 \rightarrow T_2$ was confirmed to play a considerable role in the excitation energy relaxation process of the ADPA monomer, but this influence was significantly suppressed in the hydrated ADPA-Zn^{2+} complex. These results provide additional clues for the design of new metal ion-specific fluorescence probes.

1. Introduction

During the past decades, optical sensors have been widely developed and applied in many fields, e.g. clinical diagnosis, molecular biology and biochemistry, materials, and environmental science.[1] Especially for detecting metal ions, fluorescence spectroscopy using optical sensors is recognized as the most favorable and convenient approach, according to their unique advantages, such as ion specificity, high sensitivity, and wide linear response range.[2] Scientists usually design an optical sensor for a specific metal ion, based on a principle that fluorescence of the sensor itself can be significantly enhanced with the addition of metal ions, so-called "fluorescence probes". In general, a fluorescence probe molecule consists of fluorophore, recognition and space units, in which the recognition unit plays the determinative role for ion specificity for metal ions.

For an electronically excited probe molecule, fluorescence emission and non-radiative pathways, such as internal conversion (IC) to ground state, and intersystem crossing (ISC) to nearby triplet states, competitively occur. Consequently, improving quantum yield of radiative decay or suppressing non-radiative contributions are crucial to achieve fluorescence-enhanced effects, when the probe is connected to metal ions. Photo-induced electron transfer (PET),[3] intramolecular charge transfer (ICT),[4] excited-state intramolecular proton transfer (ESIPT),[5] and aggregation-induced emission (AIE),[6] are four common mechanisms for improving fluorescence intensity through varying branching ratios of radiative and non-radiative decay paths. Although there are extensive studies on the fluorescence enhancement of metal-ion probes, the influence of these mechanisms on the IC and ISC rates of ligands are rarely mentioned. Considering that the two rates are sensitive to energy gaps between related electronic states, which might be visibly changed owing to the addition of metal ions, it gives us a motivation to quasi-quantitatively identify the influences of these action mechanisms on the non-radiative decay processes in a typical fluorescence probe system.

Among common metal elements, zinc is the second most abundant transition metal in the human physiological system, as hundreds of zinc proteins possessing one or more zinc-stabilized motifs have been identified.[8,9] Zinc deficiency is known to be associated with many diseases,[9] while excess exposure to zinc is undesirable too.[10] Therefore, fluorescent probes for Zn^{2+} ions have attracted extensive attention. However, due to close ionic radius, it is a challenge to discriminate Zn^{2+} from Cd^{2+} and Mg^{2+} ions by fluorescence sensors.[12–14] N-((anthracen-9-yl)methyl)-N-(pyridin-2-yl)pyridin-2-amine, ADPA,[15–18] whose structure is shown in Scheme 1, has been successfully applied on the specific detection of Zn^{2+} ions as an optical sensor recently.[16,19] In the presence of Zn^{2+} ions, the fluorescence intensity of ADPA was enhanced by 16-fold, in contrast to that without the metal ions. Based on theoretical calculations, Lee et al. attributed the enhancement to the chelation-enhanced fluorescence (CHEF) effect.[19,20] In the hydrated ADPA-Zn^{2+} complex, the strong fluorophore-metal interaction leads to a significant variation of molecular geometry from the ground state to the S_1 excited state. Along with the

[a] Q. Su, Y. Li, X. Zhou, S. Liu
Department of Chemical Physics, University of Science and Technology of China, Hefei, Anhui 230026, China
E-mail: xzhou@ustc.edu.cn
slliu@ustc.edu.cn

[b] J. Han, X. Zhou, S. Liu
Hefei National Research Center for Physical Sciences at the Microscale, University of Science and Technology of China, Hefei, Anhui 230026, China

Supporting information for this article is available on the WWW under https://doi.org/10.1002/cphc.202400140

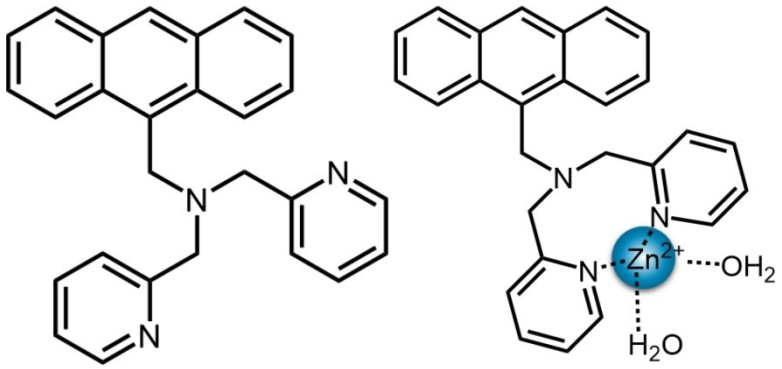

Scheme 1. Structures of ADPA monomer and hydrated ADPA-Zn^{2+} complex.

conformational change, molecular orbitals of the $S_1 \rightarrow S_0$ transition are exchanged from the one between the fluorophore and the tertiary nitrogen of the dipicolylamine unit to the normal HOMO-LUMO transition of ADPA ligand itself, thus improving fluorescence intensity significantly,[19] so-called the PET mechanism.

Notably, the "heavy-atom effect" of transition metal ions sometimes plays a considerable role for the metal-ligand interaction in improving spin-orbit coupling (SOC) and quenching fluorescence,[20] which is just opposite to the CHEF effect. That means, the influence of metal-ligand interaction on fluorescence emission needs to be thoroughly considered. Hence, the previous study of ADPA[19] was incomplete due to the lack of calculations on triplet states. Moreover, uncovering bonding characteristics between Zn^{2+} and ADPA ligand in the hydrated complex is vital for in-depth understanding the ion specificity of fluorescence sensor. Therefore, in this work, we performed new quantum chemical calculations on the ADPA monomer and hydrated ADPA-Zn^{2+} complex. Based on the optimized geometries, properties of low-lying electronic states, S_0, S_1, T_1 and T_2, were analyzed, such as excitation energies, frontier molecular orbitals and oscillator strength. The electron transfer involved in the photo-absorption and fluorescence emission processes was discussed as well using the interfragment charge transfer (IFCT) analyses.[21] In addition, the SOC and energy difference were calculated to assess the ISC contribution.

Computational Methods

All quantum chemical computations were performed using the Gaussian 16 software package.[22] B3LYP[23] and TD-DFT-B3LYP[24] were used to calculate optimized geometries and excitation energies of ADPA monomer and hydrated ADPA-Zn^{2+} complex (total charge is +2) in low-lying electronic states. The 6-311+G(d,p)[25] and SDD (Stuttgart/Dresden pseudopotentials)[26] basis sets were applied for the main group elements and transition metals, respectively. To achieve dispersion corrections, the DFT-D3 method was applied using Grimme correction.[27] The conductor-like polarizable continuum model (PCM)[28] was used to take solvent effect into account. Moreover, harmonic vibrational frequency analyses were carried out at the same level, to ensure no imaginary frequencies for all minima and to calculate zero-point energy corrections. Electron localization functions (ELF) were analyzed using Multiwfn 3.8 software[21] at the optimized geometries to study the chemical properties of metal-ligand complex. The electron (or charge) transfer percentage and local excitation percentage in the excitation and emission processes were determined with the IFCT analyses. In addition, to quantitatively calculate the ISC rate, the minimum energy crossing point (MECP) between singlet and triplet states was addressed with sobMECP program.[29,30] Then, for the calculation of accurate SOC values at the optimized geometries, $|\langle T_n|H_{SOC}|S_1\rangle|$, the all-electron basis set, def2-TZVP, was used in ORCA 5.0.1 software,[31,32] where two-electron contributions were included exactly, and the mean-field approximation within the DFT framework was used to examine electron-electron correlation.

2. Results and Discussion

2.1. Geometries and Bonding Properties

In ADPA monomer, anthracenyl and pyridyl rings play roles of the fluorophore and recognition units, respectively. Due to their relative rotations, there are three conformational isomers for the ADPA monomer with close energies and populations at room temperature. Figure S1 and Table S1 of the supporting information summarizes the corresponding calculated results of the conformers. Likewise, several stable isomers are also verified for the hydrated ADPA-Zn^{2+} complex, and the results are listed in Figure S2 and Table S2. Moreover, in order to show explicit solvent effect on the ADPA-Zn^{2+} complex structure in aqueous solutions, two or three water molecules were added to the metal-ligand complex for saturating the coordination number of Zn^{2+} ions. As shown in Figure S2, the third water molecule is located far from the central metal ion, and begins to form the second shell layer. Therefore, for the sake of simplicity, we only pay attention to the most stable one for the ADPA monomer and hydrated ADPA-Zn^{2+} complex with two bound water molecules in following discussions.

Figure 1 shows the optimized geometries of the ADPA monomer and hydrated ADPA-Zn^{2+} complex in ground state. In ADPA monomer, two pyridyl rings and anthracenyl unit are located in relatively intersecting planes, and the dihedral angles are calculated to be 64.3°, 104.7° and 43.3°, respectively (Figure 1a). Once bound to the metal ion, the molecular

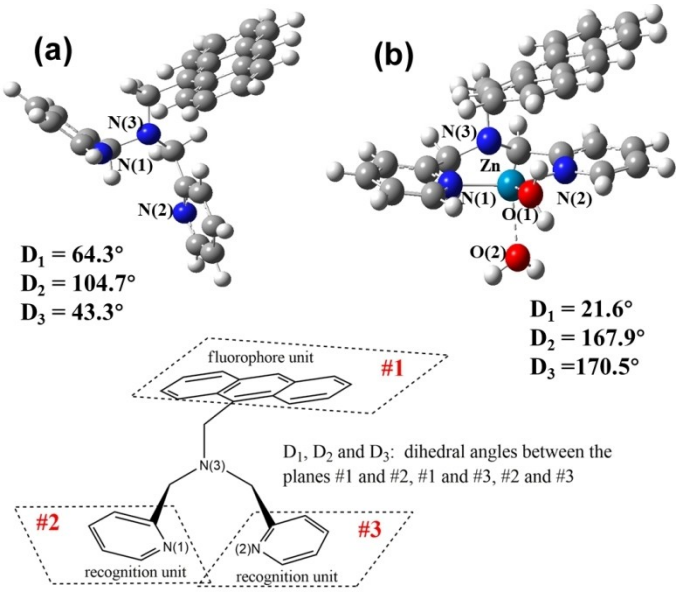

Figure 1. Optimized geometries of the ADPA monomer (a) and hydrated ADPA-Zn^{2+} complex (b) in ground state, where the main dihedral angles are noted.

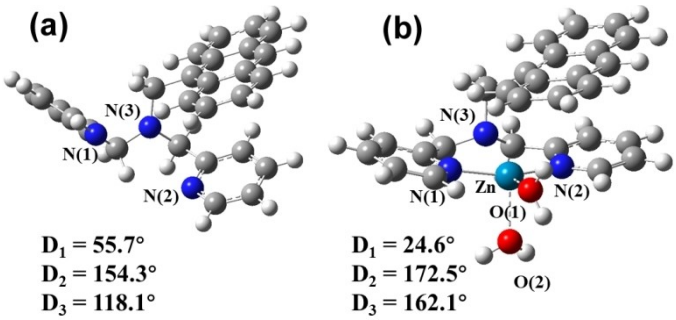

Figure 3. Optimized geometries of the ADPA monomer (a) and hydrated ADPA-Zn^{2+} complex (b) in the S_1 state, where the main dihedral angles are noted.

structure of ADPA moiety is significantly changed, especially in these dihedral angles. In the recognition units, two nitrogen atoms of pyridyl rings synergistically bind to Zn^{2+} ions by rotating their relative dihedral angles to near parallel (170.5° as shown in Figure 1b). The forming coordination bonds between Zn^{2+} and three nitrogen atoms are calculated with the distances of 2.06 Å for $R_{Zn\text{-}N(1)}$, 2.05 Å for $R_{Zn\text{-}N(2)}$, and 2.26 Å for $R_{Zn\text{-}N(3)}$, respectively. In addition, two water molecules are also coordinated to the central metal ion, and one is located at the axial and another is at the equatorial position. The distances between Zn^{2+} and two oxygen atoms are 2.10 and 2.15 Å, respectively.

Using the optimized geometry of the hydrated ADPA-Zn^{2+} complex, the electron density topological surface was analyzed, and Figure 2 shows the calculated results in the N(1)-Zn^{2+}-N(3) and O(1)-Zn^{2+}-O(2) planes, respectively. Along each N-Zn^{2+} coordinate, lone pair electrons are located in the coordination direction owing to the Zn^{2+} attraction and predominately remain on the nitrogen atom side (Figure 2a). Similar electron density distributions are verified between the metal ion and oxygen atom of water molecules (Figure 2b). All these results strongly indicate covalent properties of the forming coordination bonds between Zn^{2+} and ligands, and no obvious electron (or charge) transfer occurs during the complex formation.

Considering sufficient vibrational relaxation after photoabsorption, fluorescence photons usually are emitted from the v = 0 level of the S_1 state. In other words, the properties of fluorescence emission are mainly determined by the $S_0 \leftarrow S_1$ transition at the S_1 optimized geometry. Therefore, we calculated the optimized geometries and bonding properties of the optical-allowed lowest excited state (S_1) for the ADPA monomer and hydrated ADPA-Zn^{2+} complex ions. Figure 3 shows the calculated geometries and the main structural parameters.

In comparison to the ADPA monomer in ground state (Figure 1a), the three major dihedral angles of ADPA are changed from 64.3°, 104.7° and 43.3° in the ground state to 55.7°, 154.3° and 118.1° in the S_1 state, respectively. Meanwhile, the three C–N bonds linked to the tertiary amine rotate to the same plane in the S_1 state, accompanying with the change from

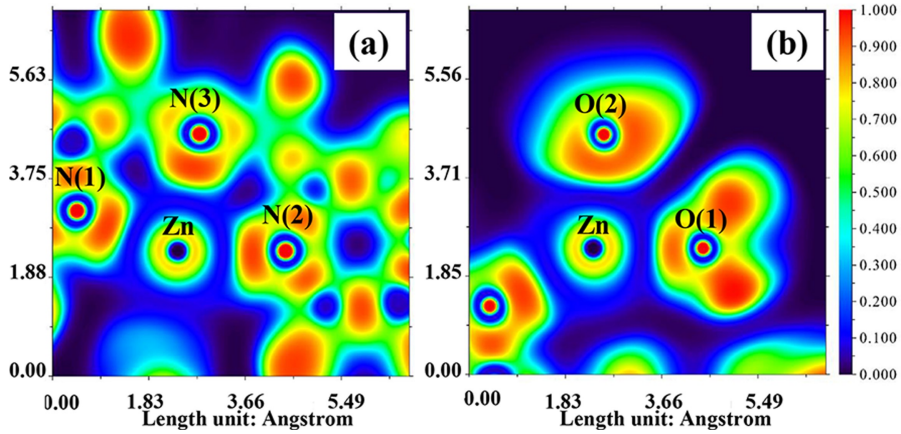

Figure 2. Electron density topological graphs of the ground-state hydrated ADPA-Zn^{2+} complex in the N(1)-Zn^{2+}-N(3) (a) and O(1)- Zn^{2+}-O(2) (b) planes, respectively.

*sp*3 to *sp*2 hybridization. As a result, two pyridyl rings lie distinctly on either side of the C–N(3)-C axis. The optimized geometry of hydrated ADPA-Zn^{2+} complex ion in the S_1 state is very close to that in ground state, except for a slightly reduced planarity of two pyridyl rings. Moreover, electron density topological surfaces (Figure S3) is almost identical to the ones in ground state, verifying the three covalent coordination bonds between Zn^{2+} and nitrogen atom of pyridyl rings. The coordination bond lengths of Zn^{2+}···N are 2.05 2.04 and 2.29 Å, and those of Zn^{2+}···O are 2.12 and 2.16 Å, respectively.

2.2. Photo-Induced Electron Transfer Mechanism

Figure 4 shows the calculated frontier molecular orbitals of the ADPA monomer and hydrated ADPA-Zn^{2+} complex ion at the optimized geometries of the S_0 and S_1 states. At the S_0 geometry, the highest occupied molecular orbital (HOMO) and the lowest unoccupied molecular orbital (LUMO) in either the monomer or the complex are both located on the anthracenyl unit (ANT). In contrast, the HOMO-1 of ADPA mainly consists of the *p* orbital of dipicolylamine (DPA), while the HOMO-1 of the complex ion is located on the ANT unit. Accordingly, the absorption to the first electronically excited state ($S_0 \rightarrow S_1$) corresponds to the $\pi \rightarrow \pi^*$ transition from HOMO to LUMO, for both ADPA monomer and hydrated ADPA-Zn^{2+}. The energy gap between HOMO and LUMO is calculated to be 3.47 eV for the ADPA monomer, and it is slightly reduced to 3.41 eV in the hydrated ADPA-Zn^{2+} ion, which is consistent with the weak red-shift of absorption observed in experiments.[18,33]

Notably, frontier molecular orbitals of the ADPA monomer in the S_1 state are significantly changed from them in ground state. As shown in Figure 4a, the energy sequence of HOMO and HOMO-1 of the ADPA monomer is reversed at the S_1 geometry, as the *p* orbital energy of tertiary amine nitrogen is significantly improved due to the *sp*3→*sp*2 hybridization change. Consequently, the HOMO→LUMO transition of the ADPA monomer (S_1) has a typical character of intramolecular electron transfer between the anthracenyl and DPA units, and the energy gap is significantly reduced to 2.69 eV. As a result, the corresponding radiative transition is dramatically weakened, which is consistent with the weak fluorescence intensity observed in experiments.[18] It is worth noting that this orbital exchange does not occur in the hydrated ADPA-Zn^{2+} complex ion as indicated in Figure 4b. The HOMO and HOMO-1 energies of the complex ion are calculated to be −5.77 and −7.29 eV,

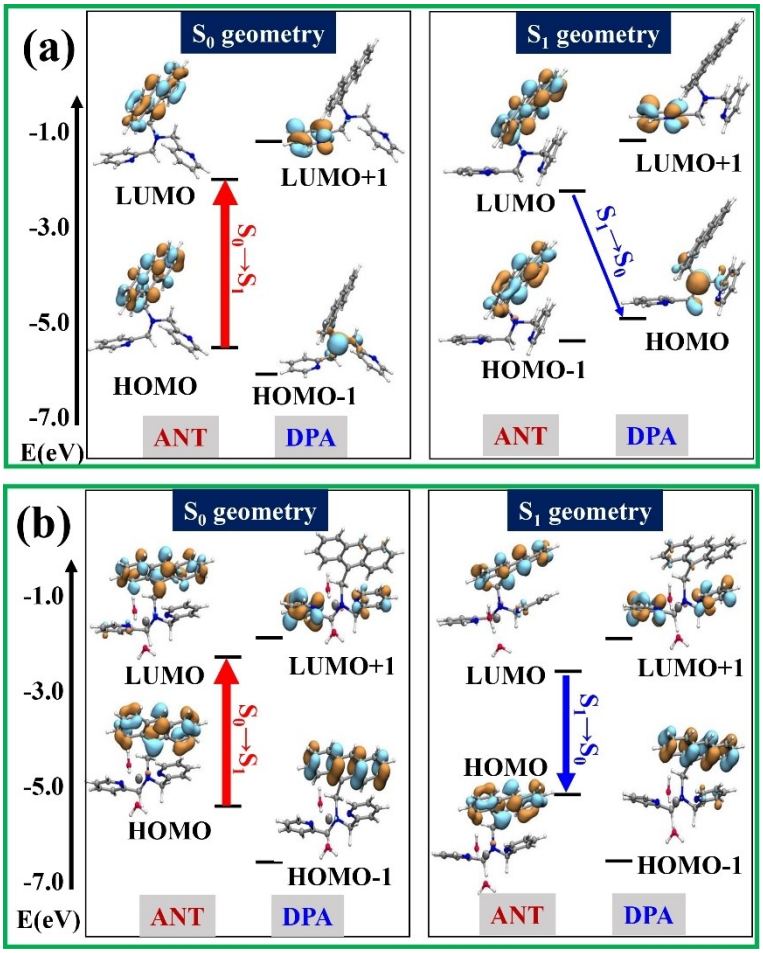

Figure 4. Frontier molecular orbitals of the ADPA monomer (upper) and hydrated ADPA-Zn^{2+} complex ions (lower) at their own optimized geometries. ANT: anthracenyl unit, DPA: dipicolylamine unit.

respectively, and their energy order is maintained as it in ground state. Thus, a relatively high fluorescence emission yield of the complex ion is expected. The current results qualitatively agree with the PET mechanism proposed by Lee et al.[19]

It is well-known that the amount of electron transferred from one fragment to another in an excitation process is crucial to quantitatively validate the PET contributions. For simplicity, we divide the probe molecule into three fragments: anthracenyl unit (ANT), tertiary amine nitrogen (TMA), and pyridyl rings (PY). Table 1 summarizes the IFCT results at the optimized geometries of the S_0 and S_1 states, respectively. In the vertical excitation process of $S_0 \rightarrow S_1$ for the ADPA monomer, the amount of transferred electrons among the three fragments all approaches zero, indicating its property of local excitation. However, along the geometry change and vibrational relaxation of the S_1 state, 0.921 electron is transferred from the ANT to TMA units in the $S_1 \rightarrow S_0$ transition at the S_1 geometry. That is, the photo-induced electron transfer definitely occurs between the ANT and TMA units of the ADPA monomer in the S_1 state, in line with the conclusion of frontier molecular orbital analyses. For the hydrated metal complex ion, only limited electron transfer is found to occur between the ANT and TMA units in the absorption and emission processes, as listed in Table 1. In addition, a very small amount of electron transfer from ANT to PY parts is also affirmed, according to the electrostatic attraction of Zn^{2+} ions. The current IFCT analyses provide quantitative evidences that the PET mechanism causes the fluorescence quenching of the ADPA monomer, while it is efficiently blocked with connecting the Zn^{2+} ion.

2.3. Internal Conversion

Although the PET mechanism provides a qualitative interpretation for the fluorescence-enhanced effect, the non-radiative processes, such as ISC, IC and IET, might also play considerable roles in the energy decay of excited molecules, competing with the electron transfer. To quantitatively evaluate their contributions in the overall decay dynamics, excitation energies and oscillator strengths at the S_0 and S_1 optimized geometries were calculated for the ADPA monomer and hydrated ADPA-Zn^{2+} complex ion, respectively, and were summarized in Table 2. As shown in Table 2, the f_{Abs} value of the $S_0 \rightarrow S_1$ transition for the ADPA monomer at the S_0 geometry is calculated to be 0.1172, which is larger than that of the hydrated ADPA-Zn^{2+} complex ion (0.0692). When the molecular structure is transformed to the S_1 geometry, the oscillator strength f_{FL} is significantly enhanced from 0.0015 to 0.1087 owing to the PET process, with the formation of the hydrated complex ion.

We know, the experimentally observed fluorescence intensity, I(λ), depends on the molar extinction coefficient ε(λ) ($\propto f_{Abs}$) and the quantum yield of fluorescence emission $\Phi_{FL}(\lambda)$, as shown in the formula (1),

$$I(\lambda) = N \cdot \varepsilon(\lambda) \cdot \Phi_{FL}(\lambda) \propto f_{Abs} \cdot \Phi_{FL}(\lambda) = f_{Abs} \cdot \frac{k_{FL}}{k_{FL} + k_{ISC} + k_{IC}} \quad (1)$$

where N is the number density of molecules, f_{Abs} and f_{FL} are the oscillator strength of absorption and fluorescence emission, k_{FL}, k_{ISC} and k_{IC} are the fluorescence radiation, ISC and IC rates, respectively. Simply, the k_{FL} and k_{IC} values can be roughly calculated with the formula (2) and (3),[34] according to the energy gap law,

Table 1. The IFCT analyses of the S_0-S_1 transition for ADPA monomer and hydrated ADPA-Zn^{2+} complex, where ΔΘ shows the amount of net electron transfer, ANT is anthracenyl unit, TMA is tertiary amine nitrogen, PY is pyridyl rings.

	state	$\Delta\Theta_{(ANT\rightarrow TMA)}$	$\Delta\Theta_{(ANT\rightarrow PY)}$	$\Delta\Theta_{(ANT\rightarrow Zn)}$	$\Delta\Theta_{(TMA\rightarrow PY)}$	$\Delta\Theta_{(TMA\rightarrow Zn)}$	$\Delta\Theta_{(PY\rightarrow Zn)}$
ADPA	S_0	-0.006	−0.006	–	−0.000	–	–
	S_1	0.921	0.039	–	−0.018	–	–
ADPA-Zn^{2+}	S_0	−0.018	0.149	0.005	0.003	0.000	0.000
	S_1	0.018	−0.180	−0.001	-0.005	0.000	0.000

Table 2. Properties of absorption (abs.) and fluorescence (fl.) transitions of the ADPA monomer and hydrated ADPA-Zn^{2+} complex, where E_{S1} is the excitation energy of the S_1 state, *f* is the oscillator strength, the configuration interaction coefficient for the transitions and the corresponding contribution are listed too.

	transition	E_{S1} (eV)/λ (nm)	*f*	assignment	coeff.	contribution
ADPA	$S_0\rightarrow S_1$ (abs.)	3.09/401	0.1172	HOMO→LUMO (ππ*)	0.7011	98%
	$S_0\rightarrow S_2$ (abs.)	3.35/370	0.0015	HOMO-1→LUMO (ππ*)	0.7032	99%
	$S_0\leftarrow S_1$ (fl.)	2.00/620	0.0015	HOMO←LUMO (nπ*)	0.7057	100%
ADPA-Zn^{2+}	$S_0\rightarrow S_1$ (abs.)	3.00/413	0.0692	HOMO→LUMO (ππ*)	0.6969	97%
	$S_0\rightarrow S_2$ (abs.)	3.30/376	0.0113	HOMO-1→LUMO (ππ*)	0.6219	77%
	$S_0\leftarrow S_1$ (fl.)	2.37/523	0.1087	HOMO←LUMO (ππ*)	0.7020	99%

$$k_{FL} = f_{FL} \cdot E_{S1}^2/1.499 \quad (2)$$

$$\log(k_{IC}/s^{-1}) \approx 12 - 2 \cdot \frac{E_{S1}}{hc} \quad (3)$$

where E_{S1} represents the S_1 excitation energy at its optimized geometry with the unit of cm^{-1}, h is Planck constant, c is the light speed in vacuum. Using the calculated f_{FL} and E_{S1} data in Table 2, the k_{FL} values are determined to be 2.60×10^5 s^{-1} and 2.65×10^7 s^{-1}, and k_{IC} were 5.94×10^8 s^{-1} and 1.50×10^8 s^{-1} for the ADPA monomer and hydrated ADPA-Zn^{2+} complex, respectively. Obviously, the k_{IC} values are much faster than k_{FL}, regardless of the ADPA monomer and the hydrated complex ion, implying the IC decay path is prominent in the overall energy decay of excited ADPA unit. Moreover, the large difference of k_{FL} between ADPA and hydrated ADPA-Zn^{2+} can be attributed to their distinct orbital compositions of the S_1 state. In ADPA, the S_1 state is comprised of nπ* orbitals, leading to minimal orbital overlap and a significant structural transition from the S_0 state. This orbital arrangement restricts the transition of $S_1 \rightarrow S_0$ according to the Franck-Condon principle and orbital overlap selection rules. Consequently, ADPA exhibits a small transition dipole moment and a weak oscillator strength. These characteristics, in tandem with the Einstein coefficients for spontaneous emission, culminate in a reduced spontaneous emission rate for ADPA. In contrast, the S_1 state of ADPA-Zn^{2+} is characterized by ππ* transitions, resulting in greater orbital overlap. Moreover, less pronounced structural changes between the S_1 and S_0 states in ADPA-Zn^{2+} cause a larger transition dipole moment and, subsequently, a higher spontaneous emission rate. Therefore, the higher fluorescence rate in hydrated ADPA-Zn^{2+} is a direct consequence of its favorable electronic transitions and structural properties.

2.4. Intersystem Crossing

In addition to the IC decay, the ISC rate (k_{ISC})[35] is affected by SOC factors[32] and Gibbs free energy gap (ΔG_{ST}) between the singlet (S_1) and neighboring triplet (T_n) states, as shown in the equation (4). The energy gap ($\Delta E_{ST} = E_{S1} - E_{Tn}$) and the SOC values of $S_1 \rightarrow T_1$ and $S_1 \rightarrow T_2$ were both calculated for the ADPA monomer and hydrated ADPA-Zn^{2+} complex at their own S_1 geometry. Table 3 lists the calculated results for the two molecules. It is worth noting that the second triplet state (T_2) has approximate excitation energy to the S_1 state, while the T_3 state is much higher (~0.99 eV, not listed in the table).

$$k_{ISC} = \frac{2\pi}{\hbar} |\langle T_n | H_{SOC} | S_1 \rangle|^2 \frac{1}{\sqrt{4\pi\lambda k_B T}} exp\left[-\frac{(\Delta G_{ST} + \lambda)^2}{4\pi\lambda k_B T}\right] \quad (4)$$

where λ is the reorganization energy determined by the energy difference between S_1 and T_n state at the optimized geometries of S_1, k_B is the Boltzmann constant, and T is the room temperature (298 K in this work).[35]

Obviously, both $S_1 \rightarrow T_1$ and $S_1 \rightarrow T_2$ processes are thermodynamically feasible for the ADPA monomer, since the corresponding ΔE_{ST} values are positive, 0.56 eV for $S_1 \rightarrow T_1$ and 0.04 eV for $S_1 \rightarrow T_2$. Specially, the small energy gap of $S_1 \rightarrow T_2$ facilitates the occurrence of near-resonant energy transfer. The calculated SOC values are relatively small as 3.22 cm^{-1} for $S_1 \rightarrow T_1$ and 0.35 cm^{-1} for $S_1 \rightarrow T_2$. Notably, the dominant electronic transition of the S_1 and T_2 states are both the nπ* configuration, while the T_1 state comprises the ππ* one. According to the El-Sayed propensity rule, the smaller SOC exists for the $S_1 \rightarrow T_2$ transition in comparison to that of $S_1 \rightarrow T_1$, in line with the currently calculated results. We would like to emphasize that based on these calculated SOC values, the ISC from the S_1 state to the two low-lying triplet states should play a non-negligible role in the excitation energy relaxation process of the ADPA monomer.

In contrast, the ΔE_{ST} value of $S_1 \rightarrow T_1$ is increased to 1.22 eV in the hydrated ADPA-Zn^{2+} complex, while the $S_1 \rightarrow T_2$ transfer is unfavorable due to the endothermic process ($\Delta E_{ST} = -0.41$ eV in Table 3). Moreover, the dominant electronic transition of the T_1 and T_2 states are both ππ* configuration, in which T_1 maintains the same orbital properties as the ADPA ligand, while one π−electron located at the anthracenyl unit is excited to the π* orbital of the pyridine group in the T_2 state. Consequently, the SOC of $S_1 \rightarrow T_1$ is very small (0.28 cm^{-1}) according to the El-Sayed rules, and that of $S_1 \rightarrow T_2$ is relatively large (1.46 cm^{-1}). Notably, the increased energy gap and the reduced SOC value for $S_1 \rightarrow T_1$ both imply that this ISC contribution is significantly weakened in the metal ion-ligand complex.

To further clarify the ISC contribution in the excitation energy decay process, the MECP between the S_1 and T_2 states was identified at the TD-DFT-B3LYP–D3/6-311G** level of theory. Figure 5a and 5b exhibits the MECP optimized geometries for the ADPA monomer and hydrated ADPA-Zn^{2+} complex ion, respectively. As shown by the geometric comparison in Figure 5c and 5d, two MECP geometries are close to those in their own S_1 state, regardless of the ADPA monomer and hydrated ADPA-Zn^{2+} complex. Specially, the MECP and T_2 structures of ADPA are also close, as shown by the minor changes of the A_1 and A_2 rotational angles. Such minor rotations imply a relatively flat potential energy surface for the ISC process. In contrast, relatively significant changes of A_1 and A_2 occur in the transformation from the MECP to the T_2 state for hydrated ADPA-Zn^{2+}, although the MECP geometry is also close to that of the T_1 state. Such the structural differences lead to the larger ΔG_{ST} and ΔE_a values in the complex ion.

Table 3. Energy difference (ΔE_{ST}) between the S_1 and nearby triplet states, together with the corresponding SOC values, at the S_1 geometries of the ADPA monomer and hydrated ADPA-Zn^{2+} complex, respectively.

	transition	ΔE_{ST}/eV	SOC/cm^{-1}
ADPA	S_1 (nπ*)→T_1 (ππ*)	0.56	3.22
	S_1 (nπ*)→T_2 (nπ*)	0.04	0.35
ADPA-Zn^{2+}	S_1 (ππ*)→T_1 (ππ*)	1.22	0.28
	S_1 (ππ*)→T_2 (ππ*)	-0.41	1.46

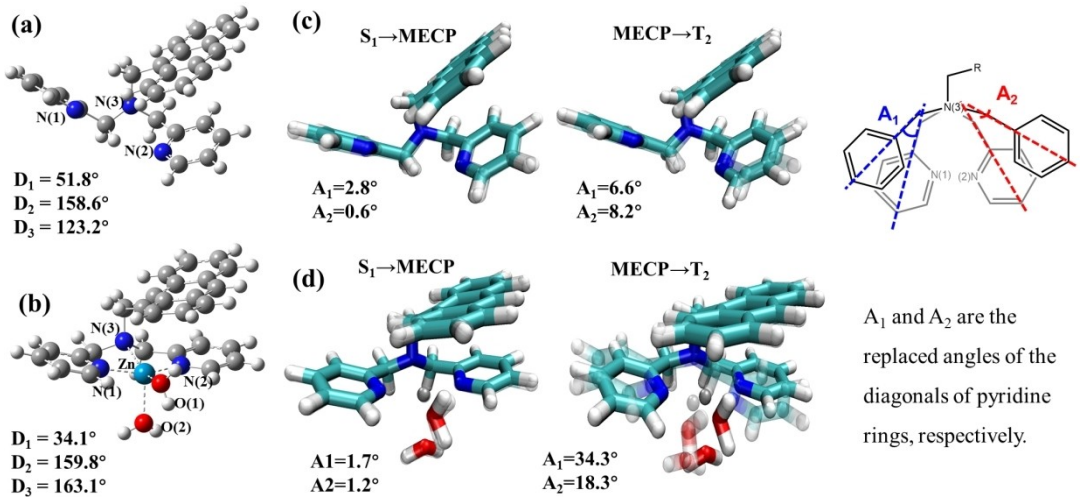

Figure 5. Optimized MECP geometries of the S_1 and T_2 states for the ADPA monomer (a) and hydrated ADPA-Zn^{2+} complex (b) in the S_1 state, while schematic of the molecular structures with controlled anthracene overlap in the ISC process of $S_1 \rightarrow MECP \rightarrow T_2$ for ADPA monomer (c) and hydrated ADPA-Zn^{2+} complex (d) is exhibited as well.

Using the MECP geometries, we calculated its dominant molecular orbital transition and corresponding ISC parameters, and summarized in Table 4. As shown in Figure 6, along the ISC process of $S_1 \rightarrow MECP \rightarrow T_2$, the $n\pi^*$ orbital transition is maintained in the ADPA monomer, while the dominant molecular orbital transition for the hydrated ADPA-Zn^{2+} complex is changed from the $\pi\pi^*$ transition of the anthracenyl unit in the S_1 state to another $\pi\pi^*$ transition involving the π^* orbital of the pyridine group. The MECP orbital transition of the complex shows a mixed state of the π^*-orbital of the anthracene unit and the π^*-orbital of the pyridine ring, providing solid evidence for its intermediate role on the ISC process of $S_1 \rightarrow T_2$.

Moreover, for the ADPA monomer, the activation energy (ΔE_a) to form MECP is only 0.03 eV. Such a small barrier, together with a negative ΔG_{ST} (−0.05 eV), strongly indicates the efficient and thermodynamically feasible ISC of $S_1 \rightarrow T_2$. Meanwhile, the SOC value is enhanced to 0.40 cm^{-1} at the MECP. In

Table 4. Gibbs free energy gap (ΔG_{ST}, in eV) between the S_1 and T_2 states, reorganization energy (λ, in eV) for the ISC process of $S_1 \rightarrow T_2$, and ISC rates (k_{ISC}, in s^{-1}) for the ADPA monomer and hydrated ADPA-Zn^{2+} complex ion, as well as the SOC values (in cm^{-1}) and activation energies ($\Delta E_a = E_{MECP} - E_{S1}$) at the MECP geometries.

	transition	ΔG_{ST}	λ	SOC	ΔE_a
ADPA	S_1 ($n\pi^*$)→T_2 ($n\pi^*$)	−0.05	0.04	0.40	0.03
ADPA-Zn^{2+}	S_1 ($\pi\pi^*$)→T_2 ($\pi\pi^*$)	0.25	0.32	0.90	0.18

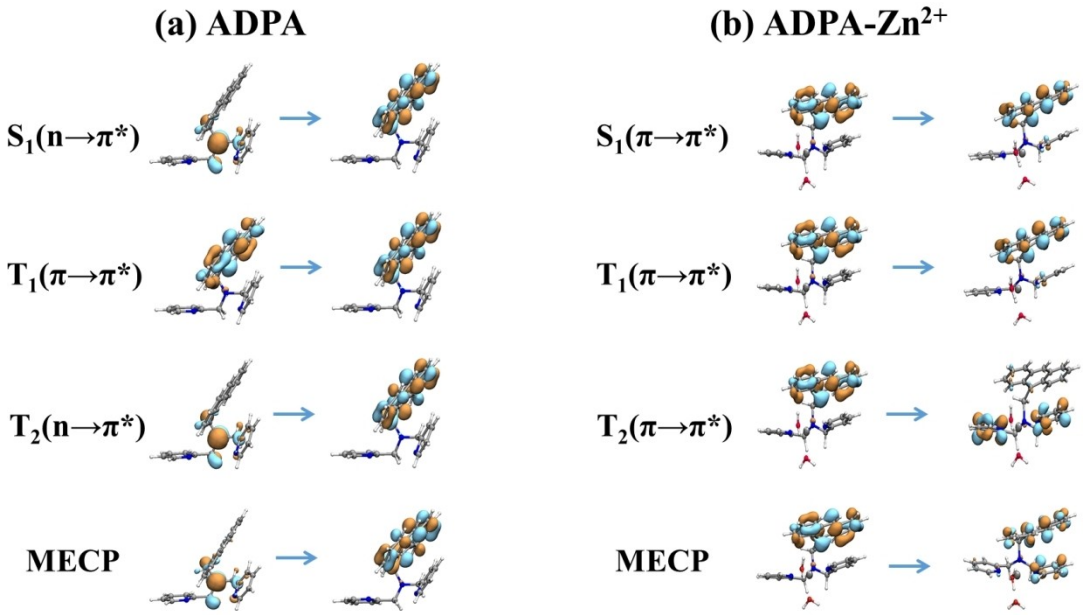

Figure 6. The dominant molecular orbital components of the S_1, T, T_2 and MECP states for the ADPA monomer (a) and hydrated ADPA-Zn^{2+} complex (b).

Table 5. The decay rates of the fluorescence emission, IC, and ISC of $S_1 \rightarrow T_2$ for the ADPA monomer and hydrated ADPA-Zn^{2+} complex ion, as well as the quantum yield of fluorescence.

	k_{FL}	k_{IC}	k_{ISC}	Φ_{FL}	$f_{Abs}\,\Phi_{FL}$
ADPA	2.60×10^{5}	5.94×10^{8}	2.04×10^{8}	3.26×10^{-4}	3.82×10^{-5}
ADPA-Zn^{2+}	2.65×10^{7}	1.50×10^{8}	6.27×10^{6}	0.145	1.00×10^{-2}

addition, a small reorganization energy λ is determined to be 0.04 eV owing to little structural deformation to produce MECP (the structural change' root mean square deviation (RMSD) is only 0.1 Å) from the S_1 state. Accordingly, the calculated k_{ISC} value is 2.04×10^{8} s^{-1}, which is much faster than its calculated k_{FL} (2.60×10^{5} s^{-1}).

In contrast, for the hydrated ADPA-Zn^{2+}, the transformation of $S_1 \rightarrow T_2$ obviously becomes an endothermic process with a positive ΔG_{ST} of 0.25 eV. Compared with the result of the ADPA monomer, the activation energy (ΔE_a) to reach MECP is 0.18 eV, indicating the existence of a visible spin-change barrier, and meanwhile the SOC value is 0.90 cm^{-1} at the MECP. Moreover, more extensive structural deformation between the S_1 and T_2 states is verified according to RMSD of 0.5 Å, leading to an increased relaxation reorganization energy ($\lambda = 0.32$ eV). Given these data, the ISC rate is significantly reduced to 6.27×10^{6} s^{-1}. In order to show more clearly the contribution of each energy decay channel, Table 5 summaries the calculated rates of each elementary process for the overall excitation energy decay.

Using the formula (1), the quantum yield of fluorescence emission (Φ_{FL}) is determined to be 3.26×10^{-4} for the ADPA monomer and 0.145 for the complex ion. Taking into account the change of absorption ability (f_{Abs}), the overall fluorescence emission efficiency should be significantly increased from 3.82×10^{-5} to 1.00×10^{-2}. Although the current level of computation is not sufficient to obtain precise excitation energies, such a tremendously enhanced trend of fluorescence efficiency can be identified. Moreover, as indicated in Table 5, the effect stems mainly from the approximately 70-fold increase of f_{FL} (in Table 2) induced by the PET mechanism. In addition, the ISC process of $S_1 \rightarrow T_2$ also exhibits a considerable influence to improve Φ_{FL} with binding to the Zn^{2+} ion, through suppressing its considerable contribution in the ADPA unit.

3. Conclusions

In this work, we performed DFT and TD-DFT calculations for low-lying electronic states of the ADPA monomer and hydrated ADPA-Zn^{2+} complex ion. Using optimized geometries, frontier molecular orbital analyses were conducted. In the ADPA monomer, HOMO and HOMO-1 energy sequence is reversed in the S_1 state compared to ground state, leading to intramolecular electron transfer between the anthracenyl and DPA units. As a result, only weak fluorescence emission is observed in the monomer due to the PET mechanism. In contrast, this reversion of molecular orbital sequence is prevented when the ADPA is connected to Zn^{2+}, and thereby the PET mechanism is significantly suppressed. Furthermore, the amount of transferred electron in the monomer and complex were determined using the IFCT analyses, providing solid and quantitative evidences for the PET mechanism.

Besides, we took into account non-radiative decay contributions in the current systems, including ISC and IC processes. Based on the calculated energies of the lowest electronic states (S_0, S_1, T_1, and T_2) and the SOC values, the ISC from the S_1 to T_2 states plays a considerable role in the relaxation of excitation energy in the ADPA monomer. However, in the hydrated ADPA-Zn^{2+} complex, this ISC process is significantly weakened. The current computations provide an in-depth understanding of the fluorescence-enhanced mechanisms of metal-ion-specific optical probes.

Author Contributions

All authors contributed to make study conception and review manuscript. The first draft is written by **Su**, and **Li**, **Han**, **Lu** review the manuscript. **Zhou** does the full instructions and revisions, and **Liu** provide the financial support.

Acknowledgements

This work was financially supported by the National Natural Science Foundation of China (Nos. 22027801 and 22073088). All DFT calculations were performed on the supercomputing system in the Supercomputing Center of the University of Science and Technology of China.

Conflict of Interests

The authors have no conflict of interest in this research.

Data Availability Statement

The data that support the findings of this study are available from the corresponding author upon reasonable request.

Keywords: optical sensor · electron transfer · intersystem crossing · fluorescence enhancement

[1] P. Roy, *Coord. Chem. Rev.* **2021**, *427*, 213562.
[2] K. Aslan, I. Gryczynski, J. Malicka, E. Matveeva, J. R. Lakowicz, C. D. Geddes, *Curr. Opin. Biotechnol.* **2005**, *16*, 55–62.
[3] M. A. Fox, *Photochem. Photobiol.* **1990**, *52*, 617–627.

[4] Z. R. Grabowski, K. Rotkiewicz, W. Rettig, *Chem. Rev.* **2003**, *103*, 3899–4032.
[5] J. Zhao, S. Ji, Y. Chen, H. Guo, P. Yang, *Phys. Chem. Chem. Phys.* **2012**, *14*, 8803–8817.
[6] Y. Hong, J. W. Y. Lam, B. Zhong Tang, *Chem. Soc. Rev.* **2011**, *40*, 5361–5388.
[7] A. Klug, D. Rhodes, *Cold Spring Harbor Symp. Quant. Biol.* **1987**, *52*, 473–482.
[8] C. Andreini, L. Banci, I. Bertini, A. Rosato, *J. Proteome Res.* **2006**, *5*, 196–201.
[9] A. S. Prasad, *BMJ* **2003**, *326*, 409–410.
[10] L. M. Plum, L. Rink, H. Haase, *Int. J. Environ. Res. Public Health* **2010**, *7*, 1342–1365.
[11] R. D. Shannon, *Acta Crystallogr. Sect. A* **1976**, *32*, 751–767.
[12] L. Wang, W. Qin, X. Tang, W. Dou, W. Liu, *J. Phys. Chem. A* **2011**, *115*, 1609–1616.
[13] D. Dakternieks, *Coord. Chem. Rev.* **1990**, 279–294.
[14] U. Basu, I. Khan, A. Hussain, P. Kondaiah, A. R. Chakravarty, *Angew. Chem. Int. Ed.* **2012**, *51*, 2658–2661.
[15] A. Ojida, Y. Mito-oka, K. Sada, I. Hamachi, *J. Am. Chem. Soc.* **2004**, *126*, 2454–2463.
[16] P. Suktanarak, S. Watchasit, K. Chitchak, N. Plainpan, K. Chainok, P. Vanalabhpatana, P. Pienpinijtham, C. Suksai, T. Tuntulani, V. Ruangpornvisuti, P. Leeladee, *Dalton Trans.* **2018**, *47*, 16337–16349.
[17] Y. Tu, J. Liu, H. Zhang, Q. Peng, J. W. Y. Lam, B. Z. Tang, *Angew. Chem. Int. Ed.* **2019**, *58*, 14911–14914.
[18] H. Lee, H.-S. Lee, J. H. Reibenspies, R. D. Hancock, *Inorg. Chem.* **2012**, *51*, 10904–10915.
[19] H. Lee, R. D. Hancock, H.-S. Lee, *J. Phys. Chem. A* **2013**, *117*, 13345–13355.
[20] Y. Wei, M. Zheng, L. Chen, X. Zhou, S. Liu, *Dalton Trans.* **2019**, *48*, 11763–11771.
[21] T. Lu, F. Chen, *J. Comput. Chem.* **2012**, *33*, 580–592.
[22] M. J. Frisch, G. W. Trucks, H. B. Schlegel, G. E. Scuseria, M. A. Robb, J. R. Cheeseman, G. Scalmani, V. Barone, G. A. Petersson, H. Nakatsuji, et al., Gaussian 16, Rev. C.01, Gaussian, Inc., Wallingford, CT, **2016**.
[23] P. J. Stephens, F. J. Devlin, C. F. Chabalowski, M. J. Frisch, *J. Phys. Chem.* **1994**, *98*, 11623–11627.
[24] E. Runge, E. K. Gross, *Phys. Rev. Lett.* **1984**, *52*, 997.
[25] G. Petersson, M. A. Al-Laham, *J. Chem. Phys.* **1991**, *94*, 6081–6090.
[26] M. Dolg, U. Wedig, H. Stoll, H. Preuss, *J. Chem. Phys.* **1987**, *86*, 866–872.
[27] S. Grimme, J. Antony, S. Ehrlich, H. Krieg, *J. Chem. Phys.* **2010**, *132*, 154104.
[28] M. F. Iozzi, B. Mennucci, J. Tomasi, R. Cammi, *J. Chem. Phys.* **2004**, *120*, 7029–7040.
[29] A. O. Lykhin, D. S. Kaliakin, G. E. DePolo, A. A. Kuzubov, S. A. Varganov, *Int. J. Quantum Chem.* **2016**, *116*, 750–761.
[30] "Tian Lu, sobMECP program," can be found under http://sobereva.com/286, (accessed 15 April 2021).
[31] F. Neese, *Wiley Interdiscip. Rev.: Comput. Mol. Sci.* **2012**, *2*, 73–78.
[32] B. de Souza, G. Farias, F. Neese, R. Izsak, *J. Chem. Theory Comput.* **2019**, *15*, 1896–1904.
[33] J. W. Nugent, H. Lee, J. H. Reibenspies, H.-S. Lee, R. D. Hancock, *Polyhedron* **2017**, *130*, 47–57.
[34] P. Klán, J. Wirz, *Photochemistry of Organic Compounds: From Concepts to Practice*, John Wiley & Sons, **2009**. pp. 35-37.
[35] R. A. Marcus, *Angew. Chem. Int. Ed. Engl.* **1993**, *32*, 1111–1121.
[36] S. Schlamminger, D. Haddad, F. Seifert, L. S. Chao, D. B. Newell, R. Liu, R. L. Steiner, J. R. Pratt, *Metrologia* **2014**, *51*, S15.

Manuscript received: February 6, 2024
Revised manuscript received: March 17, 2024
Accepted manuscript online: March 18, 2024
Version of record online: ■■, ■■

RESEARCH ARTICLE

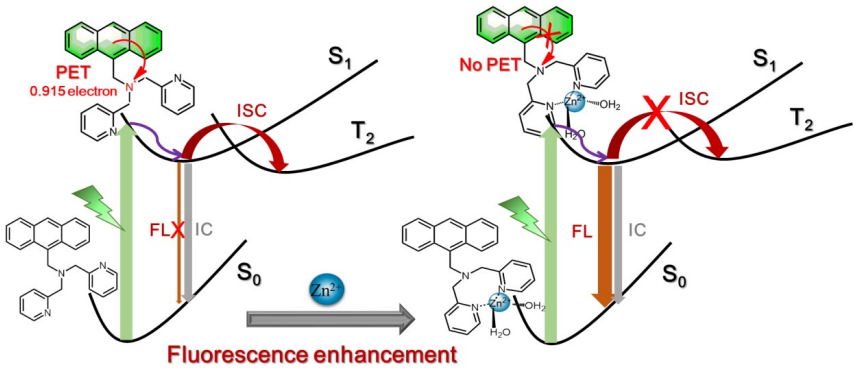

Interfragment charge transfer analyses shows the amount of transferred electrons in the ADPA-Zn^{2+} complex, providing solid evidences for the photo-induced electron transfer (PET) mechanism for its fluorescence enhancement ability, as a complement to molecular orbital analyses. Moreover, intersystem crossing (ISC) is confirmed to play a non-negligible role in the fluorescence-enhanced mechanism.

Q. Su, Y. Li, J. Han, X. Zhou, S. Liu**